Temporal scale-dependent sensitivity analysis using discrete wavelet transform and active subspaces

Daniel Bittner[1], Michael Engel[1], Barbara Wohlmuth[2,3], David Labat[4], Gabriele Chiogna[1,5]

[1]Chair of Hydrology and River Basin Management, Technical University Munich, Arcisstraße 21, 80333 Munich, Germany
[2]Chair for Numerical Mathematics, Technical University Munich, Boltzmannstraße 3, 85748 Garching near Munich, Germany
[3]Department of Mathematics, University of Bergen, Allegaten 41, 5020 Bergen, Norway
[4]Geosciences Environnement Toulouse – GET, 14, Avenue Edouard Belin, 31400 Toulouse, France
[5]Institute of Geography, University of Innsbruck, Innrain 52, 6020 Innsbruck, Austria

Key Points:

- Results show that active subspaces are temporal scale dependent
- Active subspace dimensions reflect dominant hydrological processes on different temporal scales
- Methodology provides information on temporal-scale dependent parameter sensitivities

Abstract

Global sensitivity analysis of model parameters is an important step in the development of a hydrological model. If available, time series of different variables are used to increase the number of sensitive model parameters and better constrain the model output. However, this is often not possible. To overcome this problem, we coupled the active subspace method with the discrete wavelet transform. The Haar mother wavelet is the most appropriate for this purpose in case of homoschedastic measurement error, since it avoids any loss of information through the discrete wavelet transform of the signal. With this methodology, we study how the temporal scale dependency of hydrological processes affects the structure and dimension of the active subspaces. We apply the methodology to the LuKARS model of the Kerschbaum spring discharge in Waidhofen a.d. Ybbs (Austria). Our results reveal that the dimensionality of an active subspace increases with increasing hydrologic processes which are affecting a temporal scale. As a consequence,

Corresponding author: Gabriele Chiogna, gabriele.chiogna@tum.de

different parameters are sensitive on different temporal scales. Finally, we show that the total number of sensitive parameters identified at different temporal scales is larger than the number of sensitive parameters obtained using the complete spring discharge signal. Hence, instead of using multiple data time series to identify more sensitive parameters, we can also obtain more information about parameter sensitivities from one single, decomposed time series.

1 Introduction

Uncertainty quantification constitutes an important part of hydrological modeling (Hartmann et al., 2017; Wagener & Pianosi, 2019). In particular, quantifying parametric uncertainty is important since the reliability of simulation results strongly depends on its parametrization (Beven, 1995; Reinecke et al., 2019). Within the context of parametric uncertainty, the determination of an appropriate parameter set is usually accompanied by sensitivity analyses (Borgonovo et al., 2017; Vrugt et al., 2002). Sensitivity analysis measures how much the output of a model changes by varying its inputs, e.g. spring discharge (van Werkhoven et al., 2008; Wagener & Montanari, 2011). Sensitivity analysis methods can be divided into two groups: local and global methods (Pianosi et al., 2016; Saltelli et al., 2008). In a local sensitivity analysis, parameter modifications are only performed at single locations of the parameter space (Tang et al., 2007; Saltelli et al., 2019). In contrast, parameter sensitivity is measured over the full parameter space in a global analysis (Razavi & Gupta, 2015; Song et al., 2015). Global methods are usually prefered in hydrology as they provide information on the sensitivity of one parameter in relation to others (Cloke et al., 2008; Wagener & Pianosi, 2019).

Constantine et al. (2014) and Constantine and Diaz (2017) proposed the active subspace method as a tool to perform global sensitivity analysis. Besides computing a global sensitivity metric, this method has the advantage that it further provides information on relevant linear combinations of model parameters. These relevant parameter combi-

nations can be used to efficiently construct surrogate models and perform Bayesian inversion at low computational cost (Erdal & Cirpka, 2019; Teixeira Parente et al., 2019). The active subspace method was successfully applied in several hydrological studies ranging from lumped parameter models (Bittner, Teixeira Parente, et al., 2020; Teixeira Parente et al., 2019) to distributed modeling approaches (Erdal & Cirpka, 2019, 2020; Gilbert et al., 2016). (Bittner, Teixeira Parente, et al., 2020) also showed that the features and dimension of an active subspace can find a reasonable hydrological explanation, in case of a lumped karst hydrological model. So far, the active subspace method was applied to hydrological variables that integrate processes occurring at multiple temporal scales, such as discharge and heat fluxes (Erdal & Cirpka, 2020; Jefferson et al., 2015). However, it is well known that hydrological time series can be decomposed into different temporal scales, for example using wavelet transform analysis (Grinsted et al., 2004; Labat et al., 2000b; Torrence & Compo, 1998).

Wavelet transforms determine the crucial scales of variability and localizes variations in the modes of variability within a time series (Labat, 2005). In hydrology, both continuous and discrete wavelet transform (Daubechies, 1990; Grinsted et al., 2004; Sang et al., 2013; Torrence & Compo, 1998) have been traditionally used to analyze the main scales of variability of time series (Carey et al., 2013; Coulibaly & Burn, 2004; Labat et al., 2000b; Labat, 2005; Marcolini et al., 2017; Nalley et al., 2012), their coherence with climatic and meteorological drivers (Jennings & Jones, 2015; Massei et al., 2010; Nalley et al., 2016; Schaefli et al., 2007), the impact of anthropogenic activities on the hydrological cycle (Pérez Ciria et al., 2019; Zolezzi et al., 2009), catchment classification (Agarwal et al., 2016; Pérez Ciria & Chiogna, 2020) and change point analysis (Adamowski & Prokoph, 2014). Less common is their application for the assessment of model performance (Chiogna et al., 2018; Rathinasamy et al., 2014) and model calibration (Duran et al., 2020; Schaefli & Zehe, 2009). Although several choices of the generating function, i.e. mother wavelet, are popular, it influences the resulting wavelet spectrum (Pérez Ciria et al., 2019; Schaefli et al., 2007). In particular, we focus on the decomposed signal us-

ing the discrete wavelet transform (DWT), since it is not possible to reconstruct the original signal from the coefficients derived from the continuous wavelet transform (CWT) analysis.

In this work, we study how temporal scale dependency of hydrological processes affects the structure of the active subspaces and the computed parameter sensitvities. Our hypothesis is that the active subspace dimension reflects how different linear combinations of model parameters control the simulated hydrological processes on multiple temporal scales. Moreover, we hypothesize that the sensitive parameters differ for different temporal scales of the signal, and that they can be directly related to the dominant hydrological processes of the respective temporal scales. To test these hypotheses, we couple the active subspace method with the DWT. We apply our developed methodology to a lumped karst aquifer model, i.e. LuKARS (Land use change modeling in KARSt systems), using data from the Kerschbaum springshed in Austria (Bittner et al., 2018; Bittner, Rychlik, et al., 2020). We use the same data set as used in Teixeira Parente et al. (2019), who performed sensitivity analysis using the active subspace of the Kerschbaum spring discharge signal. This allows us to compare the results obtained from the temporal scale-dependent sensitivity analysis with those obtained using the entire discharge signal. In Section 2, we provide details about the mathematical framework for coupling the active subspace method with DWT as well as a short description of the model and used data. In Section 3, we explain and discuss the results of the methodology as applied to the illustrative example of the Kerschbaum spring LuKARS model. Finally, we summarize our findings in Section 4.

2 Methodology

The methodology that we present in this work, aims at decomposing both, the modeled and the measured discharge signal at different scales using DWT and, hence, to perform an independent sensitivity analysis for each temporal scale. Then, we test if the

dimension and structure of the active subspaces identified, i.e. the sensitive physical parameters, are different among different scales. This means that we try to identify if different temporal scales of the modeled discharge signal are sensitive to changes in different model parameters. If so, we want to investigate if these scales can be approximated by an active subspace with different dimension and eigenvectors. We apply the proposed methodology to a real case study, where we use a lumped karst hydrological model, i.e. LuKARS, to model the discharge of the Kerschbaum spring in Waidhofen a.d. Ybbs (Austria). This entire process is summarized in Fig. 1. For reproducibility, the codes and data of the methodology can be downloaded from Bittner, Engel, et al. (2020).

2.1 Coupling DWT with Active Subspaces

In the following, we provide a detailed explanation of how we couple the DWT with the active subspace method. For convenience, matrices are underlined twice and vectors once. Scalars and sets are not indicated with an underline. If the output of a function G of a quantity $\bullet$ is a matrix, it is notated as $\underline{\underline{G}}(\bullet)$. We do this analogously for vectors, scalars and sets. A quantity, e.g. spring discharge time series, is considered as transformed if it was decomposed from the original to the wavelet basis. To distinguish between original and transformed quantities, $\tilde{\bullet}$ is introduced as the transformed quantity and $\hat{\bullet}$ as the approximated version of $\tilde{\bullet}$ within the transformed wavelet basis.

2.1.1 Discrete Wavelet Transform

The starting point of this work is to define a hydrological model $G(X)$ and to collect time series data $\underline{d}$ that should be simulated by the model, here the discharge of the Kerschbaum spring (Step 1 in Fig. 1). Then, the next step is to choose a DWT (Step 2 in Fig. 1), i.e. a mother wavelet, and decompose the measured and simulated discharge time series into several temporal scales using the DWT. Our measured discharge time series $\underline{d}$ consists of n data points. The natural frequency of discrete wavelet transformations is two (Walnut, 2013). Hence, n is chosen as

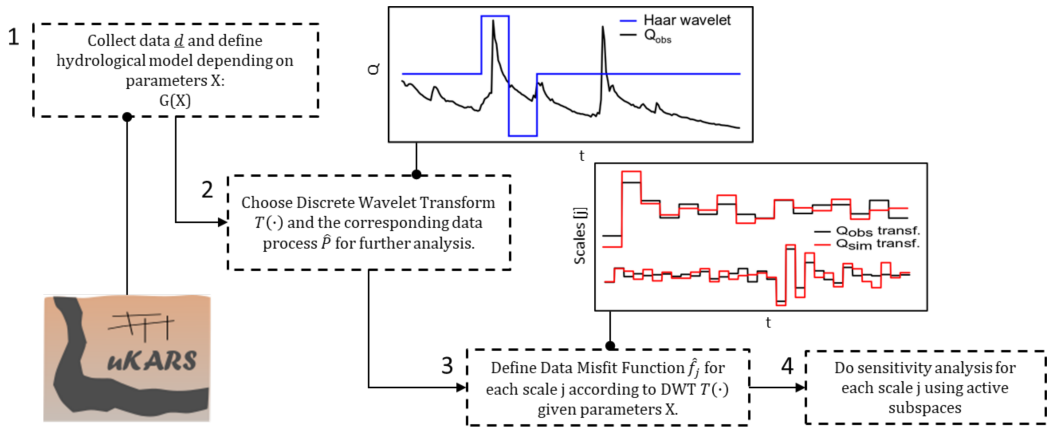

Figure 1. Flowchart of the methodology for coupling the active subspace method with the discrete wavelet transform.

$$n = 2^m, \tag{1}$$

where $m \in \mathbb{N}$. A scale j is defined as the details coefficients $\underline{\tilde{d}}_j$ corresponding to the $(m-j)$-th iteration in a filter bank (Mallat, 1989). The filter bank recursively splits the given time series in the details and approximation coefficients $\underline{\tilde{a}}_j$ as defined in Walnut (2013). This means that the details coefficients of scale j are obtained by decomposing the approximation coefficients of scale $(j+1)$. In total, we have $(m+1)$ scales. Accordingly, we define $T(\bullet)$ as the discrete wavelet transformation of the measured and modeled discharge time series:

$$\underline{\tilde{d}}_j = T_j(\underline{d}) \; \forall j = 0...m. \tag{2}$$

The transformation T gives a set of details coefficients with m members and one approximation coefficient $\tilde{a}_0$ which is referred to as the details coefficient of Scale 0 $\tilde{d}_0$. Hence, the subscript j chooses a member of the set given by T: the scale j of the transformed discharge. Thus, the decomposition of the simulated output from the hydrological model G into its temporal scales can be written as

$$\widetilde{\underline{G}}_j = T_j\left(\underline{G}\right). \tag{3}$$

2.1.2 Definition of the Data Misfit Function for different scales

The decomposition of the measured and modeled discharge time series is the most important part in our methodology since the sensitivity has to be quantified with respect to the gradient of a data misfit between measured and simulated discharge for each scale. Thus, to perform a sensitivity analysis of each scale with respect to the data misfit we need an evaluation function for each scale. Similar to Teixeira Parente et al. (2019), we define the Data Misfit Function (DMF) between the measurements $\underline{d}$ and the simulated discharge $\underline{G}(\underline{X})$ with a set of model parameters $\underline{X}$ as

$$f(\underline{X}) = \frac{1}{2}\|\underline{\underline{\Gamma}}^{-\frac{1}{2}}((\underline{d} - \mu_t) - (\underline{G}(\underline{X}) - \mu_t))\|_2^2, \tag{4}$$

where $\|\bullet\|_2^2$ is the square of the Euclidean norm. Note that the shift μ_t is the average of $\underline{d}$ with respect to time.

The DMF in Eq. 4 corresponds to a Gaussian measurement noise. It can be modeled as a discrete Gaussian Process $GP(\underline{d})$. Such a process is completely defined by its covariance matrix $\underline{\underline{\Gamma}}$ and its mean vector which should be equal to the measured data $\underline{d}$. Here, $\underline{\underline{\Gamma}}$ is a diagonal matrix describing an homoscedastic error. In this work, we consider an error on the measured discharge of 2 ls^{-1}. The advantage and the limitations of this assumption will be discussed later on. So far, we only defined the DMF within the original basis. Thus, to stay with a Gaussian model, the construction of the DMFs within the wavelet basis requires the definition of the mean vector $\underline{d}_j$ and covariance matrix $\underline{\underline{\Gamma}}_j$ for each scale j. It is important to recall that the DMF aims at quantifying the

error between model and measured values, considering that the measured values and their wavelet transform are uncertain.

For that reason, we need to ensure that the DWT of the original signal properly distributes the uncertainty among each scale. As a consequence, coupling the active subspace method with DWT requires to transform the random process as a whole in order to properly define a DMF $\tilde{f}_j(\underline{X})$ for each scale j (Step 3 in Fig. 1). The idea is to find a mother wavelet (Step 2 in Fig. 1) such that the scales are statistically independent from each other. By that, we ensure obtaining independent information about the sensitivity of the parameters from each scale without any loss of information about the uncercainty in the measurements.

The term information is used in a Shannon Entropy sense (Shannon, 1948), referring to the loss of information as the dependence between the scales. As a measure for this information loss, we introduce the Kullback-Leibler-Divergence of the whole transformed process in the wavelet domain $\tilde{P}$ and the lumped process $\hat{P}$, in which the scales are assumed to be independent. We refer to this as the Wavelet Mutual Information (WMI), since the idea is based on the approaches for obtaining the Mutual Information (MI) of random variables as described in Cover and Thomas (2012):

$$WMI(\tilde{P}) := D_{KL}(\tilde{P} \| \hat{P}). \tag{5}$$

As $\tilde{P}$ and $\hat{P}$ are discrete processes, it is feasible to model them as multivariate Probability Density Functions. Hence, the WMI for a discrete Gaussian scale process $\widetilde{GP}$ can be obtained by inserting the definition of a multivariate Gaussian into Eq. 5:

$$WMI\left(\widetilde{GP}\left(\underline{d}\right)\right) = \frac{1}{2}\left(ln\left(\frac{\det\hat{\underline{\underline{\Gamma}}}}{\det\tilde{\underline{\underline{\Gamma}}}}\right) + tr\left(\tilde{\underline{\underline{\Gamma}}}\hat{\underline{\underline{\Gamma}}}^{-1} - \underline{\underline{(I)}}\right)\right), \tag{6}$$

where $\underline{\underline{I}}$ is the identity. If the WMI is equal to 0, we do not loose any information by assuming independent scales. Accordingly, we look for a transformation T of the Gaussian measurement data $\underline{d}$ with a constant error, such that

$$WMI\left(T\left(GP(\underline{d})\right)\right) = 0 \tag{7}$$

or that the dependence error is as small as possible. Having this transformation T, we define the new DMF's for each scale $\tilde{f}_j$ with respect to the corresponding random process $\tilde{P}_j$. Note that $\tilde{f}_j$ can only be obtained if we did not loose any information. If that is the case, we obtain statistically independet scales. Otherwise only an approximative version - assuming independent scales - $\hat{f}_j$ could be used. Since the resulting process of the transformation of a discrete Gaussian Process is not necessarily Gaussian anymore, the calculation of the process in the coefficient domain $\tilde{P}$ or the WMI can be computationally demanding. It is an iterative approach obtaining a suitable wavelet transformation which maintains all information given by the data. It is possible to demonstrate (see Appendix A) that the Haar-Wavelet yields that the WMI computes to 0 for homoscedastic Gaussian errors. Nevertheless, it is important to note that for an heteroscedastic error, e.g. a non-constant diagonal covariance matrix $\underline{\underline{\Gamma}}$, the WMI might be small but does not compute to 0. For that reason, we choose a homoscedastic measurement error of 2 ls^{-1} for the proposed methodology.

For the Haar-Wavelet, the set of the new DMFs $\hat{f}$ can be looked at as $\tilde{f}$, since all computations are exact and no information is lost. Hence, they can be defined for each scale j (Step 3 in Fig. 1) as follows:

$$\tilde{f}_j(\underline{X}) = \frac{1}{2}\|\tilde{\underline{\underline{\Gamma}}}_j^{-\frac{1}{2}}((\tilde{\underline{d}}_j - \tilde{\mu}_{t\,j}) - (\tilde{\underline{G}}_j(\underline{X}) - \tilde{\mu}_{t\,j}))\|_2^2, \tag{8}$$

where $\tilde{\underline{\underline{\Gamma}}}_j$ is the covariance matrix and $\tilde{\mu}_{t\,j} = 0$ the mean vector within scale j, whereas $\tilde{\mu}_{t\,0} = \mu_t$.

For the Haar-Wavelet the transformed shift $\tilde{\mu}_t$ is equal to 0 for all scales except Scale 0. For Scale 0, this shift is equal to the quantity of the discharge signal. This follows from the splitting Lemma as stated in Walnut (2013). Nevertheless, it is not necessary to transform the shift μ_t separately. It was intrinsicly transformed by transforming the already shifted original domain measurement time series and the shifted simulated one:

$$(\tilde{\underline{d}}_j - \tilde{\mu}_{t\,j}) := T_j\left((\underline{d} - \mu_t)\right). \tag{9}$$

For the Haar-System and our measurement data of length 2^m the shifting was not necessary but for sake of completeness it shall be done here as the approach shown in this paper could be adapted onto other basis functions or time series that require such a shifting due to wavelet boundary effects padding issues. In fact, the approach shown in this paper can be done for every basis function that supports a decomposition as given in Eq. 2.

2.1.3 Active Subspaces for Sensitivity Analysis within Different Scales

Having $\tilde{f}$ and $\underline{\tilde{G}}$ we conduct the sensitivity analysis using the Active Subspace method exactly as in Teixeira Parente et al. (2019). The only difference is that this is done for the m corresponding decomposed DMFs and model outputs as input (Step 4 in Fig. 1). Accordingly, the Active Subspace method gives the eigenvectors $\underline{v}_{j,k}$ of a gradient matrix $\underline{\underline{C}}_j$ for each scale j defined as follows:

$$\underline{\underline{C}}_j = E[\nabla_X \tilde{f}_j(\underline{X}) \nabla_X \tilde{f}_j(\underline{X})^T] = \underline{\underline{W}}_j \underline{\underline{\Lambda}}_j \underline{\underline{W}}_j^T, \tag{10}$$

where $\underline{\underline{W}}_j = [\underline{v}_{j,1} \ ... \ \underline{v}_{j,n}]$ and $\underline{\underline{\Lambda}}_j = diag(\lambda_{j,1} \ ... \ \lambda_{j,n})$ having $\lambda_{j,k} \geq \lambda_{j,k+1}$. The first index j is the scale and the second denotes the eigenvector k.

Thus, the eigenvalues $\lambda_{j,k}$ are a measure for the sensitivity of the scale DMF $\tilde{f}_j$ with respect to the corresponding eigenvectors $\underline{v}_{j,k}$. Note that the eigenvectors form an orthonormal basis. They contain those linear combinations of input parameters which are most informed by the measured discharge data within scale j. Informed means that the objective function $\tilde{f}_j(\underline{X})$, measuring the deviation from observed data within scale j, is sensitive to this linear combination of parameters.

The scale sensitivity score $s_{j,i}$ of parameter x_i within scale j is calculated by

$$s_{j,i} = \sum_{k=1}^{K} \lambda_{j,k} v_{j,k,i}, \tag{11}$$

where K is the number of parameters and i denotes the parameter. Note that $s_{j,i}$ is not the global total sensitivity, where global means that the sensitivity is measured when varying all parameters simultaneously. It is solely global within scale j. For ac-

cessing the global total measure, a weighting of the gradient of the scale DMF with respect to its contribution to the gradient of the total DMF would be necessary. However, no weighting is considered in this work since our intention is to use the entire signal of the discharge for the wavelet decomposition to obtain an independent information for each time scale.

2.2 Kerschbaum spring LuKARS model

The Kerschbaum springshed is located close to the city of Waidhofen a.d. Ybbs in Austria Fig. 2. The recharge area of the mainly dolomitic karst system covers about 2.5 km^2 and can, thus, be considered as a small scale, pre-alpine catchment. Despite the small spatial scale of the recharge area, the Kerschbaum spring represents the major source of freshwater supply for the region. Fig. 3 classifies the behavior of the Kerschbaum spring by means of statistical and spectral indices. The cross-correlation between precipitation and spring discharge, shown in Fig. 3a, highlights a quick response to precipitation events after 1 day with the highest correlation coefficient r_{xy} of 0.37. Moreover, we can identify a quick decrease of r_{xy}, pointing towards a rapid propagation of the input signal (precipitation) through the aquifer (Labat et al., 2000a; Mangin, 1984). In the cross-correlation as well as in the spectral density (Fig. 3b), we can identify a sudden change in slope from 2.35 to 1.32 after 8 days. This change points towards an activation of drainage from the aquifer storage, i.e. baseflow (Larocque et al., 1998). More information about the study site are given in Bittner et al. (2018) and Narany et al. (2019).

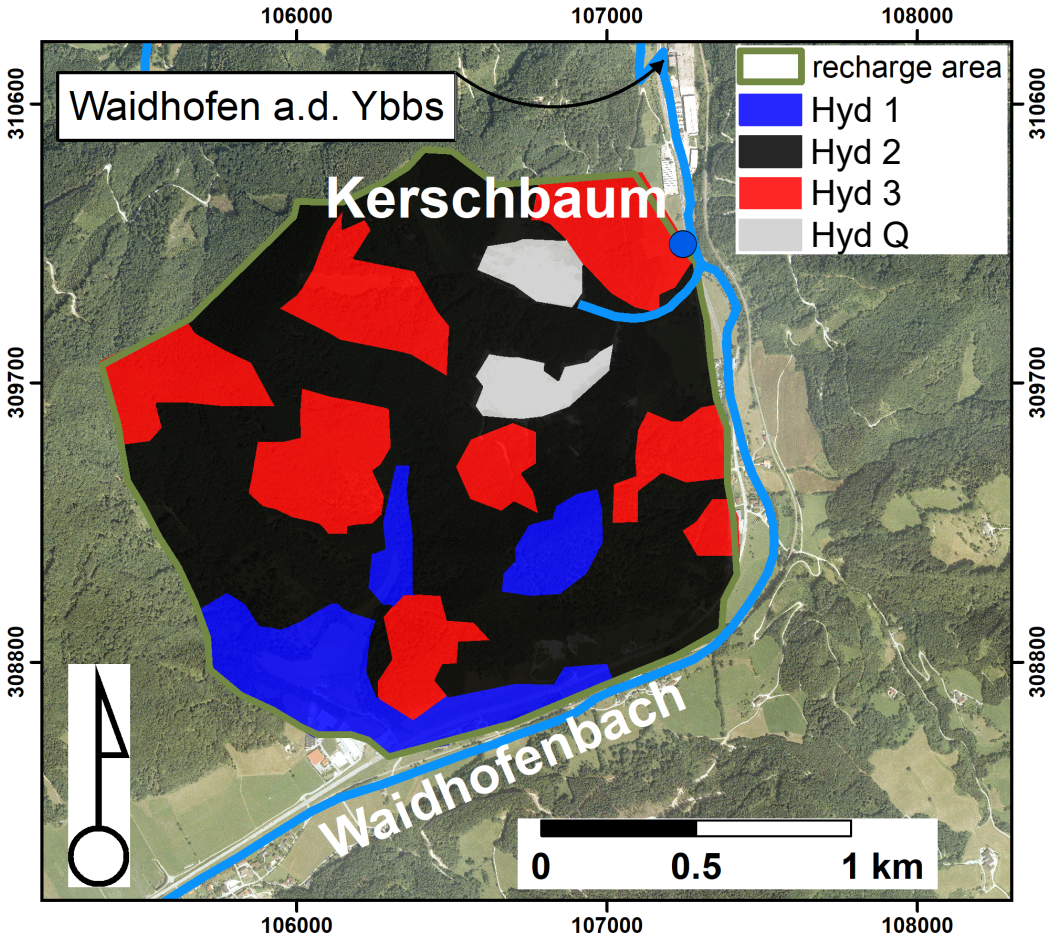

Figure 2. Recharge area of the Kerschbaum spring close to waidhofen a.d. Ybbs (Austria) including the distribution of hydrotopes, i.e. Hyd 1 (13 % of recharge area), Hyd 2 (56 % of recharge area), Hyd 3 (27 % of recharge area) and Hyd Q (4 % of recharge area). The orthophoto was kindly provided by the waterworks owner in Waidhofen a.d. Ybbs.

The LuKARS model was developed by (Bittner et al., 2018) to investigate how mining activities in the recharge area affect the quantity of discharge in the Kerschbaum spring. A GUI for the model is available as open source plugin for FREEWAT (Rossetto et al., 2018) in QGIS (Bittner, Rychlik, et al., 2020). The model is based on the implementation of hydrotopes, i.e. areas with homogeneous soil and land use characteristics (Arnold et al., 1998), shown in Fig. 2. Determined by its individual physical characteristics, each hydrotope shows a distinct repsonse to an input event, e.g. precipitation or snow melt. All hydrotopes simulate three types of flow, i.e. quickflow through conduits, groundwater recharge and secondary spring discharge. They all share one common baseflow stor-

age, i.e. the saturated zone, to which the recharge is transferred. The sum of all hydrotope quickflow responses at a given time step represents the conduit flow in the recharge area. Then, the sum of the integrated hydrotope quickflows and the baseflow simulate the spring discharge. The equations of the LuKARS model are provided in Appendix B. The model parameter ranges used in this study are shown in Table 1. Further, we use daily data for precipitation, temperature, snow depth and spring discharge in the period from January 2006 to December 2008 to run the model. It is important to note that, in order to apply the active subspace method, all model parameters need to be independent from a statistical point of view. However, in LuKARS the parameters of one hydrotope are dependent on the parameters of other hydrotopes, as shown in Eq. C1 of Appendix C. Therefore, we follow the framework proposed for the Kerschbaum LuKARS model in Teixeira Parente et al. (2019). For the seek of completeness, we include this methodology in Appendix C. Since this transformation does not have an impact on the interpretation of the results shown in the following section, it will not be further discussed.

Table 1. Overview of the model parameter ranges defined for all hydrotopes. The respective numbers indicate the lower bound and the upper bound of the parameter ranges used as prior intervals. For the meaning of the parameters, we refer to the explanation given in Appendix B.

Hydrotope	k_{hyd} [$\mathrm{m^2 d^{-1}}$]	E_{min} [mm]	E_{max} [mm]	α [-]	k_{is} [$\mathrm{m\ mm^{-1} d^{-1}}$]	k_{sec} [$\mathrm{m\ mm^{-1} d^{-1}}$]	E_{sec} [mm]
Description	discharge coef. quickflow	min. storage capacity	max. storage capacity	quickflow exponent	discharge coef. recharge	discharge coef. sec. springs	activation level sec. springs
Hyd 1	9 - 900	10 - 50	15 - 75	0.7 - 1.6	0.002 - 0.2	0.0095 - 0.95	25 - 70
Hyd 2	8.5 - 850	40 - 80	80 - 160	0.5 - 1.3	0.00055 - 0.055	0.0023 - 0.23	130 - 220
Hyd 3	7.7 - 770	75 - 120	155 - 255	0.2 - 0.7	0.00025 - 0.025	0.0015 - 0.15	320 - 450

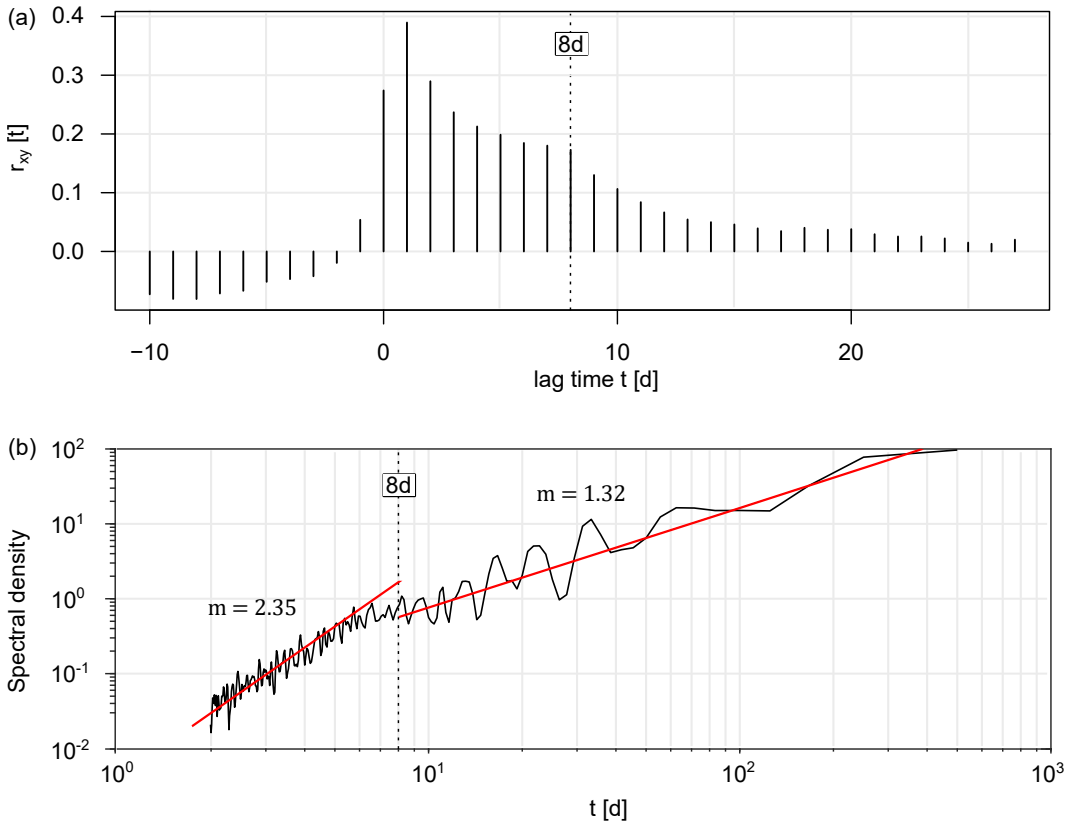

Figure 3. Time series analysis of the Kerschbaum spring discharge. a) The cross-correlation between precipitation and the spring discharge, highlighting a quick response of 1 day lag time and storage effects after 8 days. b) The spectral density of the discharge signal, also highlighting an abrupt change in spectral density of variance after 8 days, indicated by a change in slope from $m = 2.35$ to $m = 1.32$.

3 Results and discussion

In the following section, we describe and discuss the results related to the application of our methodology to the Kerschbaum LuKARS model. In detail, we discuss the dimensions of active subspaces on different scales, the scale features of the different eigenvectors as well as the hydrological meaning of identified scale dependencies. In the following, the order of scales is from the lowest to the highest frequency. To be precise, Scale 1 represents the lowest frequency, i.e. 1024 days, and Scale 10 the highest frequency, i.e. 2 days. Finally, Scale 0 represents the mean of the discharge signal.

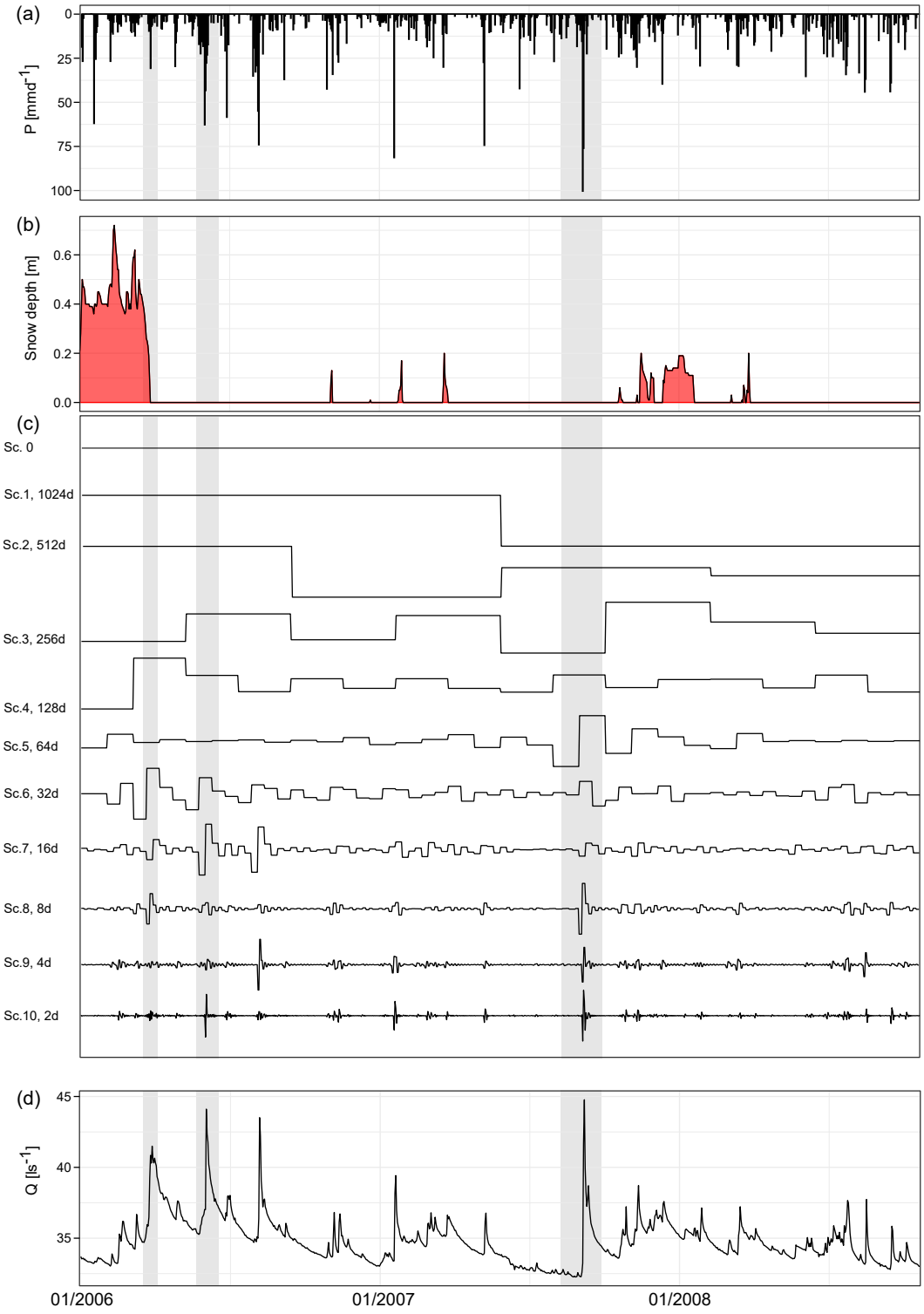

Figure 4. Data time series used in the LukARS model for the period of interest from 2006 to 2008 and the discrete wavelet scales of the measured discharge time series. a) Precipitation, b) measured snow depths, c) the discrete wavelet scales (Sc.) of the Kerschbaum spring discharge signal and d) the Kerschbaum spring discharge time series. The grey bars higlight specific peak flow events during the period of interest. Note that Scale 10 represents the highest frequency, i.e. 2 days, whereas Scale 1 represents the lowest frequency, i.e. 1024 days.

Fig. 4 shows how precipitation (Fig. 4a) and snow melt (Fig. 4b) affect the discrete wavelet scales of the Kerschbaum spring discharge (Fig. 4c) as well as the complete discharge signal (Fig. 4d). Notice that Fig. 4c does not display the values on the y-axis because they are not relevant for the following qualitative interpretation. As an example, we highlight three significant peak discharges with grey colored frames in the background. These fast spring discharges happened in response to major snow melt, e.g. April 26th, 2006, or precipitations events, e.g. June 2nd, 2006. In the DWT scales (Fig. 4c), we can observe that major input events have an effect on the spring discharge from 2 days up to a period of 8 days, which is similar to what we identified in the cross-correlation and spectral analysis (Fig. 3). Very intense input events, such as the precipitation event on September 6th, 2007, can affect even more temporal scales, up to 64 days. This is consistent for example with the observations of Schaefli et al. (2007) and other works in the literature (Charlier et al., 2015; Yang et al., 2012) and shows that when we decompose the hydrologic signal among multiple temporal scales, high flow conditions have an impact on scales larger than the event duration.

3.1 Scale dependence of active subspaces

Fig. 5a shows the decay of the eigenvalues of each wavelet scale over the first 9 eigenvalues and the truncation level. Based on our findings from the cross-correlation, spectral analysis and the DWT, we can distinguish between two groups of scales highlighted in Fig. 5a and b. Group 1 represents the sub-monthly to superannual scales, i.e. Scale 1 to Scale 7. Group 2 represents the sub-weekly to weekly, i.e. Scale 8 to Scale 10. The lower frequencies (Group 1) have active subspace dimensions between 2 and 3. In comparison, the sub-weekly to weekly scales (Group 2), representing faster spring discharge responses (Fig. 4c), only have active subspace dimensions between 1 and 2. We decided to truncate an active subspace after an eigenvalue decay over one order of magnitude. This choice, although arbitrary, does not affect the main outcomes of the analysis as discussed by Teixeira Parente et al. (2019). The eigenvalues are normalized to the maxi-

mum eigenvalue of each scale to allow for a comparability of the decays between each scale. When looking at the eigenvalue decay of each scale (Fig. 5a), we can identify that Scale 0 shows the weakest decay of all scales. Moreover, we find that with an increasing wavelet scale, the eigenvalues decay faster. The dimension of the active subspaces identified for both Group 1 and Group 2 are lower as compared to the original active subspace of the Kerschbaum LuKARS model computed without the DWT, i.e. 4 (also shown in Fig. 5b). The fact that each wavelet scale has a low dimensional active subspace indicates that fewer eigenvectors are sensitive and informed.

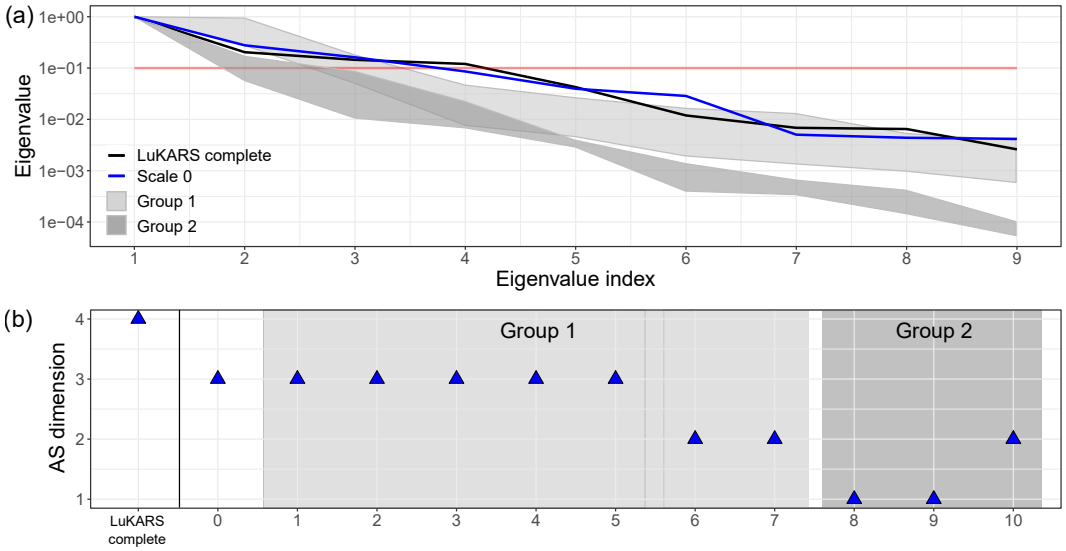

Figure 5. Active subspace dimensions. a) Eigenvalue decay of both scale groups, i.e. Group 1 representing Scale 1 to 7 and Group 2 representing Scale 8 to 10, Scale 0 and 'LuKARS complete' normalized to the maximum eigenvalue of each scale. The horizontal red line indicates the truncation level above which the active subspace is defined. b) Active subspace dimension of each discrete wavelet scale grouped in both groups of scales. 'LuKARS complete' shows the active subspace dimension when applying the active subspace method to the Kerschbaum LuKARS model without the DWT.

3.2 Eigenvector features on different scales

In Fig. 6, we show the first three eigenvectors of the complete LuKARS model (Bittner et al., 2018) and one representative scale for each group, i.e. Scale 1 for Group 1 and Scale 8 for Group 2. In the relevant eigenvectors of the complete LuKARS model (Fig. 6a), we

can observe a strong contribution of the discharge coefficient of groundwater recharge from each hydrotope, i.e. k_{is}. Moreover, we see that Hyd 2 has the highest contribution, which is the largest hydrotope in the recharge area (see Fig. 2). The second highest contribution comes from Hyd 1, representing the most dynamic hydrotope in terms of discharge variability. Although the area of Hyd 3 is larger than Hyd 1 (Fig. 2), its contribution to the first eigenvector is weakest. When further taking into account Eigenvectors 2 and 3, a similar pattern in terms of contributing hydrotopes can be observed, i.e. Hyd 1 and Hyd 2 are dominant. It can be seen that k_{hyd} of Hyd 1 and 2, which are the discharge coefficients of the quickflow, have noticeable scores in Eigenvector 2, .

Looking at the first eigenvector of Scale 0 (Fig. 6b), we also find that mainly the groundwater recharge parameters (k_{is}) of each hydrotope have the highest contribution in the first eigenvector. Moreover, we can observe the same ranking of hydrotope contributions in the first eigenvector compared to the complete LuKARS model, i.e. in decreasing order Hyd 2, Hyd 1 and Hyd 3. When further taking into account Eigenvector 2 and 3, we further notice high scores of the quickflow parameters k_{hyd} of Hyd 1 and Hyd 2.

Next, we look at the eigenvectors of Scale 1, being representative for the scales of Group 1. In all eigenvectors (Fig. 6c), we can observe a dominant contribution of Hyd 1 and Hyd 2 parameters, similar to Scale 0. In contrast to Scale 0, Hyd 1 parameters show a higher contribution as compared to those of Hyd 2. When looking at single parameter contributions in each eigenvector, we generally observe highest scores of the discharge coefficients of k_{is} and k_{hyd} of Hyd 1 and Hyd 2. Moreover, the water storage thresholds, i.e. E_{min} and ΔE (in the following referred to as the E parameters), of both dominant hydrotopes have noticeable contributions in the eigenvectors. These parameters control the onset and offset of the quickflow and, thus, further control the amount of water becoming groundwater recharge.

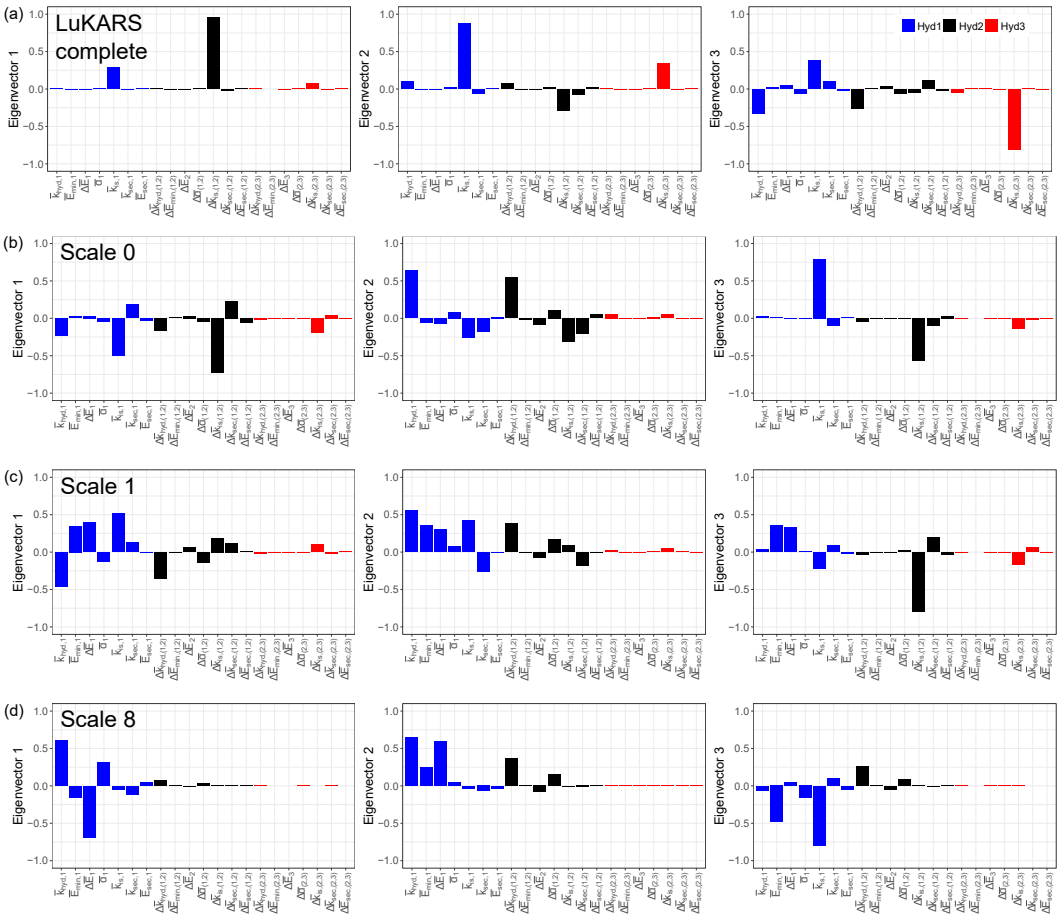

Figure 6. First three eigenvectors of Scale 0, 1 and 8. 'LuKARS complete' are the eigenvectors computed without scale dependencies.

Although we are showing the first three eigenvectors of Scale 8 (Fig. 6d), only the first eigenvector is relevant as highlighted by the active subspace dimensions in Fig. 5b. Looking at the parameters contributing to the relevant eigenvector, we notice a clear dominance of Hyd 1 parameters and negelectable scores of both other hydrotopes. In particular, k_{hyd}, the E parameters and α have the highest scores. These parameters primarily control the quickflow of Hyd 1, where α regulates the magnitude of quickflow events. In contrast to the previously discussed scales, no significant contribution from groundwater recharge controlling parameters can be noticed. These results are in a good agreement with the identified impacts of snow melt and precipitation events on the temporal scales of the spring discharge. As Hyd 1 has the highest quickflow variability, this hy-

drotope contributes most to the peakflow during these events, which explains the high importance of the quickflow parameters in Group 2 scales.

3.3 Scale-dependent parameter sensitivities

Next, we show the parameter sensitivities for each wavelet scale and the complete LuKARS model in Fig. 7a. Both, Scale 0 and the complete LuKARS model without scale dependencies have a similar pattern in terms of sensitive parameters, comparable to our findings in the eigenvectors of the dominant eigenvalues (Fig 6a and b). In particular the k_{is} parameters of each hydrotope are the most sensitive parameters with decreasing scores from Hyd 2 over Hyd 1 to Hyd 3. Looking at the sensitive parameters on the sub-monthly to superannual scales (Group 1), we can observe that Hyd 1 parameters are most sensitive in all scales. Moreover, k_{is} is the most sensitive parameter of Hyd 2 with noticeable scores in all scales of Group 1. For Hyd 3, k_{is} is only sensitive in Scale 1 and 2. In general, the most sensitive parameters in the sub-monthly to superannual scales are the discharge coefficients of the quickflow, i.e. k_{hyd}, and the recharge, i.e. k_{is}. Focussing on the parameter sensitivities of the sub-weekly to weekly scales (Group 2), no noticeable scores can be found in Hyd 2 and Hyd 3, with the only exception given by k_{hyd} and k_{is} of Hyd 2 in Scale 7. All sensitive parameters on these scales are related to Hyd 1, which are particularly those controlling the quickflow, i.e. k_{hyd}, the E parameters and α.

Fig. 7b shows the total number of sensitive parameters cumulated over all discrete wavelet scales. We start cumulating sensitive parameters at Scale 10, since it has the highest frequency and represents the quickest response of the decomposed discharge signal. We consider a parameter to be sensitive if its score is larger than 0.01. This value indicates the 0.75-quantile of all sensitivity scores computed for each scale. Parameters which are sensitive on more than one scale are counted only once in the scale of its first appearance. We observe that a total of 11 parameters are sensitive over all scales. In comparison, in the complete LuKARS model without scale dependencies, only 7 parameters are sensitive. This shows that further information about sensitive parameter can be hidden

in the temporal scales of the discharge. From a physical point of view, this can be explained by the temporal-scale dependent relevance of different hydrologic processes, for which different model parameters can be sensitive.

3.4 Hydrological interpretation

In general, we found the weakest eigenvector decay for Scale 0 and decreasing active subspace dimensions with increasing wavelet scales. As introduced in Section 2.1, Scale 0 represents the mean of the discharge signal. From a physical point of view, the mean of the spring discharge signal represents an interplay of multiple hydrological processes, which are represented in LuKARS as quickflow and baseflow. Thus, to reproduce the mean of the discharge signal, the model also needs to consider both processes. This relevance of different hydrological processes can explain that a larger dimension of the active subspace is needed to sufficiently inform the data misfit function for the mean of the discharge signal. For faster spring responses, i.e. the sub-weekly to weekly scale, we found lower dimensional active subspaces as compared to the sub-monthly to superannual scales. This finding is congruent with the results obtained by Bittner, Teixeira Parente, et al. (2020). In their synthetic test cases, they showed that spring discharge dominated by a single hydrological process displays a low dimensional active subspace (dimension between 1 and 2). However, here we did not identify such a dependence for hypothetical scnearios, but for specific temporal scales of a real spring dicharge. Thus, our results highlight that the coupling between DWT and active subspaces supports identifying those temporal scales of a spring discharge for which only a small number of eigenvectors are sensitive, e.g. 1 as in Scale 8. These high-frequency scales, i.e. the scales of Group 2, are mainly controlled by one dominant hydrological process, e.g. the quickflow from Hyd 1. Further, the coupled methodology allows to identify those temporal scales which are controlled by different hydrological processes, e.g. quickflow and groundwater recharge in Scale 8. For these scales, we found higher dimensional active subspaces, e.g. 3 dimensions for Scale 1.

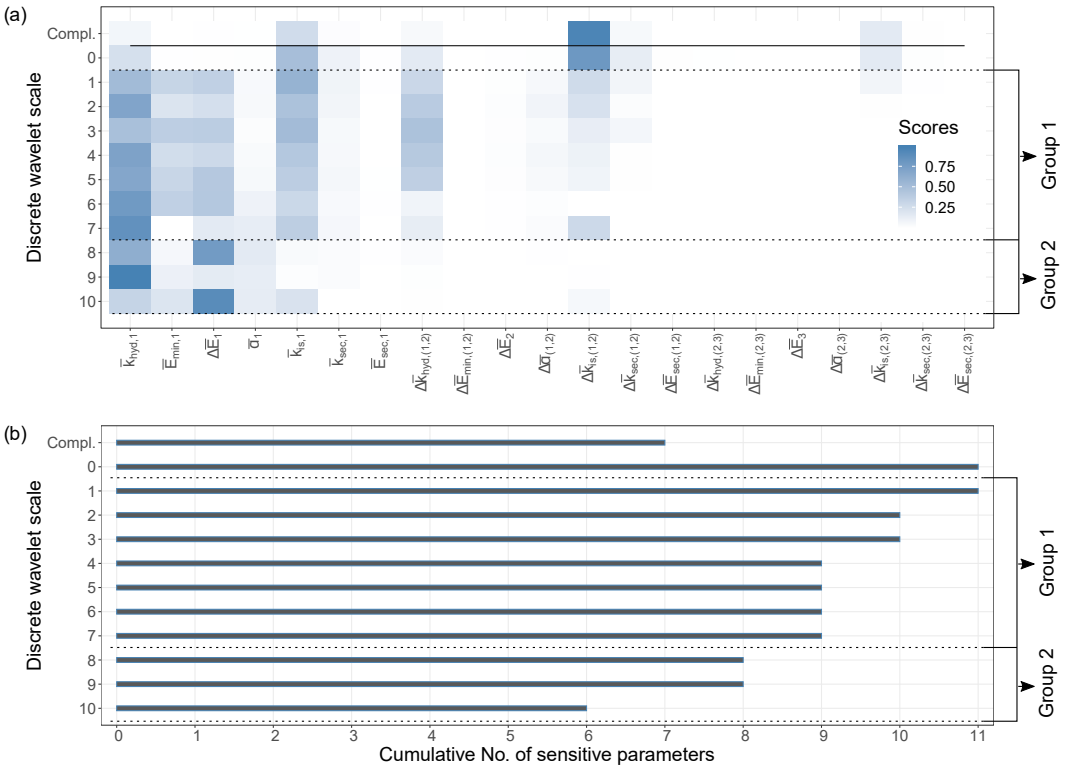

Figure 7. Scale-dependent sensitivities. a) Global sensitivities shown for each model parameter and each scale. The 'Compl' parameter sensitivities represent the sensitivity scores without scale dependencies. b) Cumulative number of sensitive parameters.

The dominant parameter contributions in Scale 0, i.e. the recharge coefficient of Hyd 2, 1 and 3 (k_{is}, Fig. 6b and Fig. 7a), are similar to those found in the dominant eigenvectors of the complete discharge signal (Teixeira Parente et al., 2019). As the major volume of the Kerschbaum spring discharge originates from baseflow (Bittner, Rychlik, et al., 2020), we argue that this is the reason why those parameters controlling the modeled baseflow, i.e. k_{is} of each hydrotope, are most sensitive in Scale 0. Moreover, k_{is} of Hyd 2 is most sensitive since Hyd 2 is the largest hydrotope in the area and contributes most to the gorundwater recharge. The noticeable scores of the quickflow parameters k_{hyd} in Scale 0 highlight that the mean of the discharge signal is composed of baseflow and quickflow contributions. In general, these findings highlight that the parameters in the dominant eigenvectors reflect the hydrological processes involved in producing the signal of a respective scale, here Scale 0.

In the scales of Group 1, the discharge coefficients of the groundwater recharge and quickflow (k_{is} and k_{hyd}) of Hyd 1 and Hyd 2 are most sensitive (Fig. 6c and Fig. 7a). As Hyd 1 is the smallest hydrotope, this finding suggests that also on the low-frequency scales of Group 1, the discharge variability of a hydrotope can play a more siginificant role than the size of a hydrotope. Taking further into account that the storage parameters of Hyd 1 and Hyd 2 (E) play an important role in Scale 1, we argue that on the sub-monthly to superannual scales, both hydrological processes, the quickflow and groundwater recharge becoming baseflow, are relevant. Similar to the findings of Schaefli et al. (2007), we can observe that some discharge peaks, caused by quickflow events in response to intense precipitation or snow melt, also affect higher periods, in our case the scales of Group 1 (Fig. 4c).

For scales of Group 2, we notice a clear dominance of quickflow controlling parameters, in particular the quickflow coefficient (k_{hyd}), the storage parameters (E) and the quickflow exponent (α), in the relevant eigenvector. This shows that on the sub-weekly to weekly scales, groundwater recharge and, thus, the baseflow does not play a significant role. This interpretation is further confirmed by the cross-correlation analysis, which highlighted a dominant contribution from quickflow up to a period of 8 days (Fig. 3a). Hence, our methodology shows that it is possible to identify those hydrological processes which are relevant for a respective temporal scale in the parameters of the relevant eigenvectors.

Finally, we can summarize that for Scale 0 and the sub-monthly to superannual scales, higher dimensional active subspaces are needed to reproduce the signals of these scales. This is due to the fact that different hydrological processes, e.g. the quickflow and the recharge becoming baseflow, from different areas in a catchment, i.e. hydrotopes, are relevant on these temporal scales. These relevant hydrological processes are reflected by the parameters contributing to each dimension of an active subspace, i.e. the eigenvectors of the dominant eigenvalues. On the contrary, only small dimensional active subspaces are needed to reproduce the signals on the sub-weekly to weekly scales. This is

related to the fact that only the quickflow from the hydrotope with high discharge variabilities, i.e. Hyd 1, matters on that temporal scale. These findings lead us to the conclusion that, for our specific case of the LukARS model, the less complex the hydrologic process structure is on a considered scale, the lower the dimensionality of the related active subspace. Thus, it is possible to identify dominant hydrological processes for different temporal scales in the dimensions of an active subspace. Moreover, our findings show that the time-scale dependence of hydrological processes, represented by the LuKARS model parameters, affects the structure of an active subspace. Furthermore, our findings in the scale-dependent parameter sensitivities are similar to what we identified in the eigenvectors of the dominant eigenvalues shown in Fig. 7a. It is interesting to observe that with an increasing scale, i.e. higher frequencies, the sensitivity of the recharge coefficients k_{is} decreases. At the same time, the sensitivity of the quickflow exponent α increases. This result indicates a clear shift in the dominant hydrological processes occuring on the respective scales, since α is the parameter that controls the intensity on which a quickflow occurs. Generally, our results of the scale-dependent parameter sensitivities support the hypothesis that parameters identified for each signal can be directly related to the hydrological processes occuring on these temporal scales.

The proposed methodology allows to discover hidden sensitive parameters in the spring discharge. To be precise, we found 11 sensitive parameters when decomposing the discharge signal, whereas only 7 where found with the complete LuKARS model (Fig. 7b). These sensitve parameters are hidden as long as the measured discharge signal is not decomposed. We show that multi-objective calibration, aiming at identifying sensitive parameters for various hydrological processes and requiring different sets of observations, is not the only way to better inform model parameters. Instead, we highlight that it is possible to obtain more information about sensitive model parameters by using only one single data time series, here spring discharge.

4 Summary

In the presented work, we coupled the active subspace method with the discrete wavelet transform. By that, we investigated the temporal scale dependencies of parameter sensitivities of a lumped karst aquifer model, LuKARS. Here, we did not give weights to the different wavelet scales, but use the entire signal of the discharge for the wavelet decomposition, such that each decomposed signal provides an independent information for the respective time scale. However, a weighting procedure can be useful if we want to favor specific hydrological conditions in model calibration. Moreover, providing a weight for each scale can help to reduce the risk of model overfitting in the solution of an inverse problem.

Although we are aware that measurement errors of hydrological time series are mostly heteroscedastic, we chose a homoscedastic error of 2 ls^{-1} for our measurement such that the WMI computes to 0. By that, we ensure not having any loss of information when decomposing our time series in the wavelet domain. Future works should focus on minimizing the loss of information when using a heteroscedastic error to account for more realistic measurement error models. This requires a normalized version of the WMI.

With the proposed methodology, we showed that the structure of an active subspace depends on the temporal scale for which it was identified. In particular, we identified two to three dimensional active subspaces for sub-monthly to superannual temporal scales and only one to two dimensional active subspaces for the sub-weekly to weekly scales. This shows that the more hydrological processes are relevant for one particular scale, the higher the dimensionality of an active subspace. For the sub-monthly to superannual temporal scales, we found that the parameters controlling the slow flowing groundwater recharge and quickflow are most important. For the sub-weekly to weekly scales, the most sensitive parameters are solely related to the quickflow of one hydrotope. Thus, the relevant linear combinations of parameters of an active supsace translate into the dominant hydrological processes for each temporal scale. Moreover, the dimensionality of an

active subspace provides a measure for the complexity of hydrologic process structure on a given temporal scale.

Finally, we were able to show that within the proposed methodology, it is possible to identify parameter sensitivities which are hidden in the temporal scales of a measured discharge signal. Hence, we do not necessarily need multiple data time series to identify more sensitive parameters in a multi-objective calibration approach. Instead, we can also obtain more information about parameter sensitivities from one single, decomposed time series.

Appendix A Haar Wavelet

In the following, we show how the decomposition using the Haar-Wavelet is done maintaining all information from the measured data. The transformation corresponding to the details $\tilde{\underline{d}}_{j-1}$ and approximation coefficients $\tilde{\underline{a}}_{j-1}$ of a time series $\underline{d}$ can be written as a linear transform:

$$\begin{bmatrix} \tilde{\underline{a}}_j \\ \tilde{\underline{d}}_j \end{bmatrix} = \begin{bmatrix} \underline{\underline{H}}(j) \\ \underline{\underline{G}}(j) \end{bmatrix} \tilde{\underline{a}}_{j+1}, \tag{A1}$$

$$\underline{\underline{H}}(j) = \frac{1}{\sqrt{2}} \begin{bmatrix} 1 & 1 & 0 & & \cdots & & 0 \\ 0 & 0 & 1 & 1 & 0 & \cdots & 0 \\ & & & \vdots & & & \\ 0 & & \cdots & & 0 & 1 & 1 \end{bmatrix}, \; j = 1...m, \tag{A2}$$

$$\underline{\underline{G}}(j) = \frac{1}{\sqrt{2}} \begin{bmatrix} 1 & -1 & 0 & & \cdots & & 0 \\ 0 & 0 & 1 & -1 & 0 & \cdots & 0 \\ & & & \vdots & & & \\ 0 & & \cdots & & 0 & 1 & -1 \end{bmatrix}, \; j = 1...m, \tag{A3}$$

where the approximation matrix $\underline{\underline{H}}(j)$ and the details matrix $\underline{\underline{G}}(j)$ are real $[2^{j-1}$ x $2^j]$ matrices. For implementation details of $\underline{\underline{H}}(j)$ and $\underline{\underline{G}}(j)$, we refer to Ryan et al. (2019). Recall that $\tilde{\underline{a}}_1$ shall be referred to as the Scale 0 details coefficients $\tilde{\underline{d}}_0$, whereas the approximation $\tilde{\underline{a}}_0$ and, hence, $\underline{\underline{H}}(0)$ is not existing. Accordingly we define:

$$\underline{\underline{G}}(0) = \underline{\underline{1}} \in \mathbb{R}^{1x1}. \tag{A4}$$

As the approximation coefficients in the Haar-System always give the energy preserving average within the corresponding interval for a scale j dyadic step function (Walnut, 2013), Scale 0 can be looked at as the mean of a signal. Since the algorithm starts with the original time series, the first approximation is the data itself:

$$\tilde{\underline{a}}_{m+1} = \underline{d} \tag{A5}$$

As a consequence, the transformation T of a time series $\underline{d}$ for getting the scale j coefficients $\tilde{d}_{ji}$ at scale interval i can be written as a nested linear transform

$$\tilde{d}_{ji} = G(j)_{i\alpha} \left(\prod_{l=0}^{m-j-1} \underline{\underline{H}}(m-l) \right)_{\alpha\beta} d_\beta, \tag{A6}$$

where greek letters subscript the dimensions which are affected by the sum-convention. Thus, the resulting scale process is a discrete Gaussian process as well. This allows the use of the same type of DMF as in Teixeira Parente et al. (2019) for all wavelet scales. Accordingly, $\widetilde{GP}(\underline{d})$ is completely defined by the transformed data $\underline{\tilde{d}}$ and the covariance matrix $\underline{\underline{\tilde{\Gamma}}}$. The relations for these quantities can be obtained by inserting the decomposition as in Eq. A6 into the common definitions of mean and covariance, respectively:

$$\tilde{\mu}_{ji} = \tilde{d}_{ji} = G(j)_{i\alpha} \left(\prod_{l=0}^{m-j-1} \underline{\underline{H}}(m-l) \right)_{\alpha\beta} \mu_\beta, \tag{A7}$$

$$\tilde{\Gamma}_{jiuw} = G(j)_{i\alpha} \left(\prod_{l=0}^{m-j-1} \underline{\underline{H}}(m-l) \right)_{\alpha\beta} \Gamma_{\beta\gamma} \, G(u)_{w\delta} \left(\prod_{l=0}^{m-u-1} \underline{\underline{H}}(m-l) \right)_{\delta\gamma}. \tag{A8}$$

Here j and u are subscripts for the scale. The indices i and w indicate the number of the coefficient within a scale. Hence, the covariance matrix $\tilde{\Gamma}$ can be looked at as a four dimensional matrix describing the m scale-covariance matrices and the covariance between them for $j \neq u$. For the Haar-Wavelet the matrix is sparse with some special properties for diagonal matrices $\underline{\underline{\Gamma}}$ which arise from $\underline{\underline{H}}$ and $\underline{\underline{G}}$. For further information about this, we refer to studies of such covariance matrices as in Vannucci and Corradi (1999). It can be shown that for a decomposition as in Eq. A8, $\underline{\underline{\tilde{\Gamma}}}$ is a constant diagonal matrix if $\underline{\underline{\Gamma}}$ is. Hence, $\underline{\underline{\tilde{\Gamma}}}$ is equal to the lumped matrix $\underline{\underline{\hat{\Gamma}}}$. Since the Haar system provides orthogonal basis functions and, hence, the decomposition in Eq. A8 is a nested orthogonal change of basis, our constant diagonal covariance matrix even remains unchanged. This obviates the need for decomposing the covariance matrix for independent homoscedastic errors:

$$\hat{\underline{\underline{\Gamma}}} = \tilde{\underline{\underline{\Gamma}}} = \underline{\underline{\Gamma}}. \tag{A9}$$

Inserting Eq. A9 in Eq. 6 the WMI of the homoscedastic Gaussian measurement error computes to zero. The scales can be assumed to be independent from each other. Recall the assumption of an homoscedastic measurement error within 2.1.2. For heteroscedastic errors $\tilde{\underline{\underline{\Gamma}}}$ might be sparse but not diagonal and consequently not equal to $\hat{\underline{\underline{\Gamma}}}$ anymore - even for the Haar-Wavelet. There would be m off-diagonal diagonals. As a consequence the DMFs could only be defined approximately.

Appendix B Model equations

LuKARS is based on the implementation of hydrotopes. Each hydrotope i represents a distinct bucket that is balanced for each time step n using the following equation:

$$E_{i,n+1} = \max[0, E_{i,n} + (S_{i,n} - \frac{Q_{\mathrm{hyd},i,n} + Q_{\mathrm{sec},i,n} + Q_{\mathrm{is},i,n}}{a_i})\,\Delta t] \tag{B1}$$

Here, E_i represents the water level [L] in hydrotope i. S_i is the mass balance of all possibke sinks and sources in a recharge area, in our case the mass balance of precipitation, snow melt, evapotranspiration and interception. For our case study, we use interception estimates provided in DVWK (1996). Further, snow melt and retention are considered using a temperature index model proposed by Martinec (1960). Finally, evapotranspiration is computed using the method of Thornthwaite (1948). Each hydrotope i has three flow components, i.e. the quickflow ($Q_{\mathrm{hyd},i}$ [$\mathrm{L^3T^{-1}}$]), secondary spring discharge ($Q_{\mathrm{sec},i}$ [$\mathrm{L^3T^{-1}}$]) and groundwater recharge ($Q_{\mathrm{is},i}$ [$\mathrm{L^3T^{-1}}$]). The absolute area covered by a hydrotope is given by a_i [$\mathrm{L^2}$].

The groundwater recharge is transferred to the baseflow storage B, for which the following balance equation is solved for each time step n:

$$E_{\mathrm{b},n+1} = \max[0, E_{\mathrm{b},n} + (\frac{\Sigma(Q_{\mathrm{is},i,n}) - Q_{\mathrm{b},n}}{A})\,\Delta t] \tag{B2}$$

The water level [L] in the baseflow storage is defined as E_{b}. The sum of the groundwater recharge coming from each hydrotope is indicated by $\Sigma(Q_{\mathrm{is},i})$ [$\mathrm{L^3T^{-1}}$]. Then, the Q_{b} [$\mathrm{L^3T^{-1}}$] represents the flow from storage B to the spring, representing the baseflow from the phreatic aquifer. The absolute area of the recharge area is given by A [$\mathrm{L^2}$].

In LuKARS, the quickflow $Q_{\mathrm{hyd},i}$ is computed based on a non-linear transfer function, which we define as follows:

$$Q_{\mathrm{hyd},i,n} = a_i\,\frac{k_{\mathrm{hyd},i}}{l_{\mathrm{hyd},i}}\,\varepsilon_n[\frac{\max(0, E_{i,n} - E_{\mathrm{min},i})}{E_{\mathrm{max},i} - E_{\mathrm{min},i}}]^{\alpha_i} \tag{B3}$$

Here, $E_{\mathrm{max},i}$ [L] and $E_{\mathrm{min},i}$ [L] are the upper and lower storage thresholds of hydrotope i. The specific discharge parameter for the quickflow is given by $k_{\mathrm{hyd},i}$ [$\mathrm{L^2T^{-1}}$]. $l_{\mathrm{hyd},i}$ [L] represents the mean distance of hydrotope i to the spring, thus, accounting for the relative location of a specific hydrotope in a recharge area. The ratio between $k_{\mathrm{hyd},i}$ and $l_{\mathrm{hyd},i}$ indicates the hydrotope discharge coefficient. A hydrotope-specific exponent of the quickflow is given by α_i. Finally, the dimensionless connectivity/activation indicator ε defines whether $Q_{\mathrm{hyd},i}$ is active or not. It is defined as

$$\varepsilon_{n+1} = 0 \text{ if } \begin{cases} \varepsilon_n = 0 \;\&\; E_{i,n+1} < E_{\mathrm{max},i} \text{ or} \\ \varepsilon_n = 1 \;\&\; E_{i,n+1} \leq E_{\mathrm{min},i} \end{cases} \tag{B4}$$

$$\varepsilon_{n+1} = 1 \text{ if } \begin{cases} \varepsilon_n = 0 \ \& \ E_{i,n+1} \geq E_{\max,i} \text{ or} \\ \varepsilon_n = 1 \ \& \ E_{i,n+1} > E_{\min,i} \end{cases} \tag{B5}$$

All other flow components are calculated using linear transfer laws, i.e.

$$Q_{\text{sec},i,n} = a_i \, k_{\text{sec},i} \, \max(0, E_{i,n} - E_{\text{sec},i}) \tag{B6}$$

$$Q_{\text{is},i,n} = a_i \, k_{\text{is},i} \, E_{i,n} \tag{B7}$$

and

$$Q_{\text{b},n} = A \, k_{\text{b}} \, E_{\text{b},n} \tag{B8}$$

where $E_{\text{sec},i}$ [L] represents the activation level for a secondary spring discharge. $k_{\text{sec},i}$ [LT^{-1}], $k_{\text{is},i}$ [LT^{-1}] and k_{b} [LT^{-1}] indicate the discharge parameters of $Q_{\text{sec},i}$ [L^3T^{-1}], $Q_{\text{is},i}$ [L^3T^{-1}] and Q_{b} [L^3T^{-1}], respectively.

Appendix C Statistical independence of LuKARS model parameters

Depending on the specific physical characteristics of each LuKARS hydrotope, their respective parameters need to be considered dependently. This means, e.g., if a hydrotope has shallow soils with coarse grained soil texture, it should have lower values for storage parameters as compared to deep and fine-textured soils. For that reason, we need to introduce the following parameter constraints, i.e. the dependencies between each hydrotope:

$$
\begin{aligned}
k_{\mathrm{hyd},1} &\geq k_{\mathrm{hyd},2} \geq k_{\mathrm{hyd},3}, \\
E_{\mathrm{min},1} &\leq E_{\mathrm{min},2} \leq E_{\mathrm{min},3}, \\
E_{\mathrm{max},1} &\leq E_{\mathrm{max},2} \leq E_{\mathrm{max},3}, \\
\alpha_1 &\geq \alpha_2 \geq \alpha_3, \\
k_{\mathrm{is},1} &\geq k_{\mathrm{is},2} \geq k_{\mathrm{is},3}, \\
k_{\mathrm{sec},1} &\geq k_{\mathrm{sec},2} \geq k_{\mathrm{sec},3}, \\
E_{\mathrm{sec},1} &\leq E_{\mathrm{sec},2} \leq E_{\mathrm{sec},3}.
\end{aligned}
\tag{C1}
$$

These constraints lead to a statistical dependence between the hydrotope model parameters. However, to use the active subspace method, statistically independent parameters are required. Hence, we need to introduce a set of calibration parameters to overcome this limitation. Here, we define three types of non-normalized calibration parameters with parameter density ρ, which can be chosen based on prior knowledge about the respective parameters. For the ranges of all discharge parameters, i.e. k_{hyd}, k_{is} and k_{sec} (in the following referred to as k_* parameters), we assumed a logarithmic distribution ρ. In contrast, a uniform prior distribution was assumed for all all other calibration parameters.

To take into account the log distribution of the k_* parameters, we define

$$
k_*^{\log} = \log(k_*) \tag{C2}
$$

for each $k_* \in \{k_{\mathrm{hyd},i}, k_{\mathrm{is},i}, k_{\mathrm{sec},i}\}$, $i = 1, 2, 3$.

Since $E_{\mathrm{min},i} \leq E_{\mathrm{max},i}$ for in all hydrotopes, $E_{\mathrm{max},i}$ is always dependent on samples taken for $E_{\mathrm{min},i}$. Hence, we define $E_{\mathrm{max},i} = E_{\mathrm{min},i} + \Delta E_i$ and replace $E_{\mathrm{max},i}$ by ΔE_i. Then, ΔE_i is independent of $E_{\mathrm{min},i}$.

To further consider the differences between two successive hydrotopes, we define new (non-normalized) calibration parameters. In the following, parameters indicated with a Δ represent new normalized calibration parameters. They take values in [0,1] and replace their corresponding model parameters. It has to be ensured that the calibration parameters are selected such that their corresponding model parameters are within their predefined ranges.

$$
\begin{aligned}
k^{\log}_{\mathrm{hyd},i} &= k^{\log}_{\mathrm{hyd},i,\mathrm{lb}} + \Delta k^{\log}_{\mathrm{hyd},(i-1,i)}(\min\{k^{\log}_{\mathrm{hyd},i,\mathrm{ub}}, k^{\log}_{\mathrm{hyd},i-1}\} - k^{\log}_{\mathrm{hyd},i,\mathrm{lb}}),\\
E_{\mathrm{min},i} &= \max\left\{E_{\mathrm{min},i-1}, E_{\mathrm{min},i,\mathrm{lb}}\right\}\\
&\qquad + \Delta E_{\mathrm{min},(i-1,i)}\left(E_{\mathrm{min},i,\mathrm{ub}} - \max\left\{E_{\mathrm{min},i-1}, E_{\mathrm{min},i,\mathrm{lb}}\right\}\right),\\
\alpha_i &= \alpha_{i,\mathrm{lb}} + \Delta\alpha_{(i-1,i)}\left(\min\left\{\alpha_{i,\mathrm{ub}}, \alpha_{i-1}\right\} - \alpha_{i,\mathrm{lb}}\right),\\
k^{\log}_{\mathrm{is},i} &= k^{\log}_{\mathrm{is},i,\mathrm{lb}} + \Delta k^{\log}_{\mathrm{is},(i-1,i)}(\min\{k^{\log}_{\mathrm{is},i,\mathrm{ub}}, k^{\log}_{\mathrm{is},i-1}\} - k^{\log}_{\mathrm{is},i,\mathrm{lb}}),\\
k^{\log}_{\mathrm{sec},i} &= k^{\log}_{\mathrm{sec},i,\mathrm{lb}} + \Delta k^{\log}_{\mathrm{sec},(i-1,i)}(\min\{k^{\log}_{\mathrm{sec},i,\mathrm{ub}}, k^{\log}_{\mathrm{sec},i-1}\} - k^{\log}_{\mathrm{sec},i,\mathrm{lb}}),\\
E_{\mathrm{sec},i} &= \max\left\{E_{\mathrm{sec},i-1}, E_{\mathrm{sec},i,\mathrm{lb}}\right\}\\
&\qquad + \Delta E_{\mathrm{sec},(i-1,i)}\left(E_{\mathrm{sec},i,\mathrm{ub}} - \max\left\{E_{\mathrm{sec},i-1}, E_{\mathrm{sec},i,\mathrm{lb}}\right\}\right),
\end{aligned}
\tag{C3}
$$

The lower bounds ($_{\mathrm{lb}}$) and upper bounds ($_{\mathrm{ub}}$) of each model parameter interval are defined in Table 1. In our case, Hyd 1 acts a as the reference hydrotope. Thus, we need to introduce new synthetic parameters only for the other hydrotopes, i.e. Hyd 2 and 3. Moreover, all non-normalized calibration parameters are normalized. This means that they are mapped to the interval [-1,1]. Given the described normalization methodology, we define the final 21-dimensional vector $\boldsymbol{x}$ of calibration parameters as follows:

$$\begin{aligned}\boldsymbol{x} = (&\bar{k}^{\log}_{\mathrm{hyd},1}, \bar{E}_{\mathrm{min},1}, \Delta\bar{E}_1, \alpha_1, \bar{k}_{\mathrm{is},1}, \bar{k}_{\mathrm{sec},1}, \bar{E}_{\mathrm{sec},1},\\ &\Delta\bar{k}^{\log}_{\mathrm{hyd},(1,2)}, \Delta\bar{E}_{\mathrm{min},(1,2)}, \Delta\bar{E}_2, \Delta\bar{\alpha}_{(1,2)},\\ &\Delta\bar{k}_{\mathrm{is},(1,2)}, \Delta\bar{k}_{\mathrm{sec},(1,2)}, \Delta\bar{E}_{\mathrm{sec},(1,2)},\\ &\Delta\bar{k}^{\log}_{\mathrm{hyd},(2,3)}, \Delta\bar{E}_{\mathrm{min},(2,3)}, \Delta\bar{E}_3, \Delta\bar{\alpha}_{(2,3)},\\ &\Delta\bar{k}_{\mathrm{is},(2,3)}, \Delta\bar{k}_{\mathrm{sec},(2,3)}, \Delta\bar{E}_{\mathrm{sec},(2,3)})^\top \in \mathbf{R}^{21}.\end{aligned} \tag{C4}$$

Acknowledgments

This collaborative research is a result of the UNMIX project (UNcertainties due to boundary conditions in predicting MIXing in groundwater), which is supported by the Deutsche Forschungsgemeinschaft (DFG) through the TUM International Graduate School for Science and Engineering (IGSSE), GSC 81. Daniel Bittner and Gabriele Chiogna refer to the Interreg Central Europe project boDEREC-CE funded by ERDF. Daniel Bittner and David Labat acknowledge financial support in form of the Procope scholarship by the French Ministry of Europe and Foreign Affairs. Gabriele Chiogna further acknowledges the support of the Stiftungsfonds für Umweltökonomie und Nachhaltigkeit GmbH (SUN). Additional financial support for Gabriele Chiogna and Barbara Wohlmuth was provided by the German Research Foundation (DFG) in the Project Hydromix (WO671/11-1). The authors further thank the water works Waidhofen a.d. Ybbs for providing the relevant spatial and time series data. Datasets and source codes for this research are available in this in-text data citation reference: Bittner, Engel, et al. (2020) (shared under the Creative Commons Attribution CC BY).

References

Adamowski, J., & Prokoph, A. (2014). Determining the amplitude and timing of streamflow discontinuities: A cross wavelet analysis approach. *Hydrological processes*, *28*(5), 2782–2793.

Agarwal, A., Maheswaran, R., Sehgal, V., Khosa, R., Sivakumar, B., & Bernhofer, C. (2016). Hydrologic regionalization using wavelet-based multiscale entropy method. *Journal of Hydrology*, *538*, 22–32.

Arnold, J. G., Srinivasan, R., Muttiah, R. S., & Williams, J. R. (1998). Large area hydrologic modeling and assessment part i: model development 1. *JAWRA Journal of the American Water Resources Association*, *34*(1), 73–89.

Beven, K. (1995). Linking parameters across scales: subgrid parameterizations and scale dependent hydrological models. *Hydrological processes*, *9*(5-6), 507–525.

Bittner, D., Engel, M., Wohlmuth, B., Labat, D., & Chiogna, G. (2020). Discrete wavelet transform coupled with the active subspace method. *HydroShare*. doi: https://doi.org/10.4211/hs.4901a0d654334c259f4ff9b49dc0a74e

Bittner, D., Narany, T. S., Kohl, B., Disse, M., & Chiogna, G. (2018). Modeling the hydrological impact of land use change in a dolomite-dominated karst system. *Journal of Hydrology*, *567*, 267–279.

Bittner, D., Rychlik, A., Klöffel, T., Leuteritz, A., Disse, M., & Chiogna, G. (2020). A gis-based model for simulating the hydrological effects of land use changes on karst systems–the integration of the lukars model into freewat. *Environmental Modelling & Software*, 104682.

Bittner, D., Teixeira Parente, M., Mattis, S., Wohlmuth, B., & Chiogna, G. (2020). Identifying relevant hydrological and catchment properties in active subspaces: An inference study of a lumped karst aquifer model. *Advances in Water Resources*, *135*, 103472.

Borgonovo, E., Lu, X., Plischke, E., Rakovec, O., & Hill, M. C. (2017). Making the most out of a hydrological model data set: Sensitivity analyses to open the model black-box. *Water Resources Research*, *53*(9), 7933–7950.

Carey, S. K., Tetzlaff, D., Buttle, J., Laudon, H., McDonnell, J., McGuire, K., ... Shanley, J. (2013). Use of color maps and wavelet coherence to discern seasonal and interannual climate influences on streamflow variability in northern

catchments. *Water Resources Research*, *49*(10), 6194–6207.

Charlier, J.-B., Ladouche, B., & Maréchal, J.-C. (2015). Identifying the impact of climate and anthropic pressures on karst aquifers using wavelet analysis. *Journal of Hydrology*, *523*, 610–623.

Chiogna, G., Marcolini, G., Liu, W., Pérez Ciria, T., & Tuo, Y. (2018). Coupling hydrological modeling and support vector regression to model hydropeaking in alpine catchments. *Science of The Total Environment*, *633*, 220–229.

Cloke, H., Pappenberger, F., & Renaud, J.-P. (2008). Multi-method global sensitivity analysis (mmgsa) for modelling floodplain hydrological processes. *Hydrological Processes: An International Journal*, *22*(11), 1660–1674.

Constantine, P. G., & Diaz, P. (2017). Global sensitivity metrics from active subspaces. *Reliability Engineering & System Safety*, *162*, 1–13.

Constantine, P. G., Dow, E., & Wang, Q. (2014). Active subspace methods in theory and practice: applications to kriging surfaces. *SIAM J. Sci. Comput.*, *36*(4), A1500–A1524. doi: 10.1137/130916138

Coulibaly, P., & Burn, D. H. (2004). Wavelet analysis of variability in annual canadian streamflows. *Water Resources Research*, *40*(3).

Cover, T. M., & Thomas, J. A. (2012). *Elements of information theory*. John Wiley & Sons.

Daubechies, I. (1990). The wavelet transform, time-frequency localization and signal analysis. *IEEE transactions on information theory*, *36*(5), 961–1005.

Duran, L., Massei, N., Lecoq, N., Fournier, M., & Labat, D. (2020). Analyzing multi-scale hydrodynamic processes in karst with a coupled conceptual modeling and signal decomposition approach. *Journal of Hydrology*, *583*, 124625.

DVWK. (1996). Ermittlung der Verdunstung von Land- und Wasserflächen. *DVWK-Merkblatt*, *238/1996*.

Erdal, D., & Cirpka, O. A. (2019). Global sensitivity analysis and adaptive stochastic sampling of a subsurface-flow model using active subspaces. *Hydrology and*

Earth System Sciences, *23*(9), 3787–3805.

Erdal, D., & Cirpka, O. A. (2020). Improved sampling of behavioral subsurface flow model parameters using active subspaces. *Hydrology and Earth System Sciences Discussions*, 1–12.

Gilbert, J. M., Jefferson, J. L., Constantine, P. G., & Maxwell, R. M. (2016). Global spatial sensitivity of runoff to subsurface permeability using the active subspace method. *Advances in water resources*, *92*, 30–42.

Grinsted, A., Moore, J. C., & Jevrejeva, S. (2004). Application of the cross wavelet transform and wavelet coherence to geophysical time series. *Nonlinear Processes in Geophysics*, *11*(5/6), 561–566.

Hartmann, A., Barberá, J. A., & Andreo, B. (2017). On the value of water quality observations for karst model parameterization. *Hydrol. Earth Syst. Sci.*, *21*, 5971–5985.

Jefferson, J. L., Gilbert, J. M., Constantine, P. G., & Maxwell, R. M. (2015). Active subspaces for sensitivity analysis and dimension reduction of an integrated hydrologic model. *Computers & Geosciences*, *83*, 127–138.

Jennings, K., & Jones, J. A. (2015). Precipitation-snowmelt timing and snowmelt augmentation of large peak flow events, western c ascades, o regon. *Water Resources Research*, *51*(9), 7649–7661.

Labat, D. (2005). Recent advances in wavelet analyses: Part 1. a review of concepts. *Journal of Hydrology*, *314*(1-4), 275–288.

Labat, D., Ababou, R., & Mangin, A. (2000a). Rainfall–runoff relations for karstic springs. part i: convolution and spectral analyses. *Journal of hydrology*, *238*(3-4), 123–148.

Labat, D., Ababou, R., & Mangin, A. (2000b). Rainfall–runoff relations for karstic springs. part ii: continuous wavelet and discrete orthogonal multiresolution analyses. *Journal of hydrology*, *238*(3-4), 149–178.

Larocque, M., Mangin, A., Razack, M., & Banton, O. (1998). Contribution of cor-

726 relation and spectral analyses to the regional study of a large karst aquifer
727 (charente, france). *Journal of hydrology*, *205*(3-4), 217–231.
728 Mallat, S. G. (1989). A theory for multiresolution signal decomposition: the wavelet
729 representation. *IEEE transactions on pattern analysis and machine intelli-*
730 *gence*, *11*(7), 674–693.
731 Mangin, A. (1984). Pour une meilleure connaissance des systèmes hydrologiques à
732 partir des analyses corrélatoire et spectrale. *Journal of hydrology*, *67*(1-4), 25–
733 43.
734 Marcolini, G., Bellin, A., Disse, M., & Chiogna, G. (2017). Variability in snow depth
735 time series in the adige catchment. *Journal of Hydrology: Regional Studies*, *13*,
736 240–254.
737 Martinec, J. (1960). The degree-day factor for snowmelt runoff forecasting. *IUGG*
738 *General Assembly of Helsinki, IAHS Commission of Surface Waters*, *51*, 468–
739 477.
740 Massei, N., Laignel, B., Deloffre, J., Mesquita, J., Motelay, A., Lafite, R., & Durand,
741 A. (2010). Long-term hydrological changes of the seine river flow (france)
742 and their relation to the north atlantic oscillation over the period 1950–2008.
743 *International journal of Climatology*, *30*(14), 2146–2154.
744 Nalley, D., Adamowski, J., & Khalil, B. (2012). Using discrete wavelet transforms
745 to analyze trends in streamflow and precipitation in quebec and ontario (1954–
746 2008). *Journal of Hydrology*, *475*, 204–228.
747 Nalley, D., Adamowski, J., Khalil, B., & Biswas, A. (2016). Inter-annual to inter-
748 decadal streamflow variability in quebec and ontario in relation to dominant
749 large-scale climate indices. *Journal of hydrology*, *536*, 426–446.
750 Narany, T. S., Bittner, D., Disse, M., & Chiogna, G. (2019). Spatial and temporal
751 variability in hydrochemistry of a small-scale dolomite karst environment. *En-*
752 *vironmental Earth Sciences*, *78*(9), 273.
753 Pérez Ciria, T., & Chiogna, G. (2020). Intra-catchment comparison and classifi-

cation of long-term streamflow variability in the alps using wavelet analysis. *Journal of Hydrology*, 124927.

Pérez Ciria, T., Labat, D., & Chiogna, G. (2019). Detection and interpretation of recent and historical streamflow alterations caused by river damming and hydropower production in the adige and inn river basins using continuous, discrete and multiresolution wavelet analysis. *Journal of Hydrology*, *578*, 124021.

Pianosi, F., Beven, K., Freer, J., Hall, J. W., Rougier, J., Stephenson, D. B., & Wagener, T. (2016). Sensitivity analysis of environmental models: A systematic review with practical workflow. *Environmental Modelling & Software*, *79*, 214–232.

Rathinasamy, M., Khosa, R., Adamowski, J., Ch, S., Partheepan, G., Anand, J., & Narsimlu, B. (2014). Wavelet-based multiscale performance analysis: An approach to assess and improve hydrological models. *Water Resources Research*, *50*(12), 9721–9737.

Razavi, S., & Gupta, H. V. (2015). What do we mean by sensitivity analysis? the need for comprehensive characterization of "global" sensitivity in e arth and e nvironmental systems models. *Water Resources Research*, *51*(5), 3070–3092.

Reinecke, R., Foglia, L., Mehl, S., Herman, J. D., Wachholz, A., Trautmann, T., & Döll, P. (2019). Spatially distributed sensitivity of simulated global groundwater heads and flows to hydraulic conductivity, groundwater recharge, and surface water body parameterization. *Hydrology & Earth System Sciences*, *23*(11).

Rossetto, R., De Filippis, G., Borsi, I., Foglia, L., Cannata, M., Criollo, R., & Vázquez-Suñé, E. (2018). Integrating free and open source tools and distributed modelling codes in gis environment for data-based groundwater management. *Environmental Modelling & Software*, *107*, 210–230.

Ryan, Ø., Ryan, & Peters. (2019). *Linear algebra, signal processing, and wavelets–a unified approach*. Springer.

Saltelli, A., Aleksankina, K., Becker, W., Fennell, P., Ferretti, F., Holst, N., ... Wu, Q. (2019). Why so many published sensitivity analyses are false: A systematic review of sensitivity analysis practices. *Environmental modelling & software*, *114*, 29–39.

Saltelli, A., Ratto, M., Andres, T., Campolongo, F., Cariboni, J., Gatelli, D., ... Tarantola, S. (2008). *Global sensitivity analysis: the primer*. John Wiley & Sons.

Sang, Y.-F., Wang, Z., & Liu, C. (2013). Discrete wavelet-based trend identification in hydrologic time series. *Hydrological Processes*, *27*(14), 2021–2031.

Schaefli, B., Maraun, D., & Holschneider, M. (2007). What drives high flow events in the swiss alps? recent developments in wavelet spectral analysis and their application to hydrology. *Advances in Water Resources*, *30*(12), 2511–2525.

Schaefli, B., & Zehe, E. (2009). Hydrological model performance and parameter estimation in the wavelet-domain. *Hydrology and Earth System Sciences*, *13*(ARTICLE), 1921–1936.

Shannon, C. E. (1948). A mathematical theory of communication. *Bell system technical journal*, *27*(3), 379–423.

Song, X., Zhang, J., Zhan, C., Xuan, Y., Ye, M., & Xu, C. (2015). Global sensitivity analysis in hydrological modeling: Review of concepts, methods, theoretical framework, and applications. *Journal of hydrology*, *523*, 739–757.

Tang, Y., Reed, P., Wagener, T., & van Werkhoven, K. (2007). Comparing sensitivity analysis methods to advance lumped watershed model identification and evaluation. *Hydrology and Earth System Sciences*, *11*(2), 793–817.

Teixeira Parente, M., Bittner, D., Mattis, S. A., Chiogna, G., & Wohlmuth, B. (2019). Bayesian calibration and sensitivity analysis for a karst aquifer model using active subspaces. *Water Resources Research*, *55*(8), 7086–7107.

Thornthwaite, C. W. (1948). *An approach toward a rational classification of climate* (Vol. 66) (No. 1). LWW.

Torrence, C., & Compo, G. P. (1998). A practical guide to wavelet analysis. *Bulletin of the American Meteorological society*, *79*(1), 61–78.

Vannucci, M., & Corradi, F. (1999). Covariance structure of wavelet coefficients: theory and models in a bayesian perspective. *Journal of the Royal Statistical Society: Series B (Statistical Methodology)*, *61*(4), 971–986.

van Werkhoven, K., Wagener, T., Reed, P., & Tang, Y. (2008). Characterization of watershed model behavior across a hydroclimatic gradient. *Water Resources Research*, *44*(1).

Vrugt, J. A., Bouten, W., Gupta, H. V., & Sorooshian, S. (2002). Toward improved identifiability of hydrologic model parameters: The information content of experimental data. *Water Resources Research*, *38*(12), 48–1.

Wagener, T., & Montanari, A. (2011). Convergence of approaches toward reducing uncertainty in predictions in ungauged basins. *Water Resources Research*, *47*(6).

Wagener, T., & Pianosi, F. (2019). What has global sensitivity analysis ever done for us? a systematic review to support scientific advancement and to inform policy-making in earth system modelling. *Earth-science reviews*.

Walnut, D. F. (2013). *An introduction to wavelet analysis*. Springer Science & Business Media.

Yang, C., Yu, Z., Hao, Z., Zhang, J., & Zhu, J. (2012). Impact of climate change on flood and drought events in huaihe river basin, china. *Hydrology Research*, *43*(1-2), 14–22.

Zolezzi, G., Bellin, A., Bruno, M., Maiolini, B., & Siviglia, A. (2009). Assessing hydrological alterations at multiple temporal scales: Adige river, italy. *Water Resources Research*, *45*(12).